Revision 1

1 Melt Inclusion CO_2 Contents, Pressures of Olivine Crystallization, and the Problem of

2 Shrinkage Bubbles

3

4 Paul J. Wallace[1], Vadim S. Kamenetsky[2], Pablo Cervantes[3,*]

5

6 1. Dept. of Geological Sciences, University of Oregon, Eugene, OR 97403

7 2. School of Physical Sciences, University of Tasmania, Hobart, Tasmania 7001, Australia

8 3. Dept. of Geology and Geophysics, Texas A&M University, College Station, TX 77845

9 * Present Address: BP America, Inc.

10

11 **Abstract**

12 The H_2O and CO_2 contents of melt inclusions can potentially be used to infer pressures of

13 crystallization and inclusion entrapment because the solubility of mixed H_2O-CO_2 vapor has

14 been determined experimentally for a wide range of melt compositions. However, melt

15 inclusions commonly develop a shrinkage bubble during post-entrapment cooling and

16 crystallization because these processes cause a pressure drop in the inclusion. This pressure drop

17 causes a vapor bubble to nucleate, leading to exsolution of low-solubility CO_2 from the trapped

18 melt. To investigate the loss of CO_2 into such bubbles, we experimentally heated large, naturally

19 glassy melt inclusions in olivine (Fo88.1 ± 0.2) from a Mauna Loa picrite in order to

20 rehomogenize the inclusions. Rapid heating to 1420°C using a high-temperature heating stage

21 dissolved the shrinkage bubbles into the melt. CO_2 contents measured by FTIR spectroscopy

22 and recalculated for melt in equilibrium with the olivine host are 224-505 ppm (n=11) for heated

23 inclusions, much higher than the CO_2 contents of naturally quenched inclusions from the same

1

Revision 1

24 sample (38-158 ppm; n=8). Pressures of inclusion entrapment calculated from the H_2O and CO_2

25 data for the heated inclusions range from 0.5 to 1.1 kbar, indicating that Mg-rich olivine

26 crystallized at very shallow depths beneath the surface of Mauna Loa. Our results indicate that

27 40-90% (average 75%) of the original CO_2 dissolved in the melt at the time of inclusion

28 entrapment can be lost to the shrinkage bubble during post-entrapment cooling. We show that

29 the computational method of Riker (2005), which predicts the pre-eruption shrinkage bubble size

30 as a function of the difference between trapping temperature and pre-eruption temperature,

31 successfully reproduces our experimental results. Our results demonstrate that the mass of CO_2

32 contained in shrinkage bubbles must be considered in order to accurately infer original pressures

33 of crystallization for melt inclusions. However, the effect is expected to be smaller for more

34 H_2O-rich melt inclusions than those studied here because the vapor bubble in such inclusions

35 will have lower mole fractions of CO_2 than the low-H_2O inclusions in our study.

36

37 **Introduction**

38   As magma ascends to the Earth's surface, dissolved volatiles are lost from the melt as a

39 result of decompression because they have pressure-dependent solubility. This makes it difficult

40 to investigate the volatile contents of magma by direct analysis of erupted material. Melt

41 inclusions are small volumes of silicate melt that are trapped inside of phenocrysts at depth

42 before eruption. Because the host crystal acts like a tiny pressure vessel, melt inclusions remain

43 at higher pressure than the ambient melt surrounding the crystals as magma moves towards the

44 surface and erupts. As a result, analysis of melt inclusions can potentially provide a record of

45 magmatic conditions, including dissolved volatile components, at the time of crystal growth

46 (e.g., Lowenstern, 1995; Danyushevsky et al., 2002; Metrich and Wallace, 2008). However, after

47   entrapment, the pressure inside of melt inclusions commonly decreases as a result of both

48   crystallization along the melt-host interface and the greater thermal contraction of the melt

49   compared with the host mineral (Roedder, 1979; Anderson, 1974; Lowenstern, 1995). In

50   addition, post-entrapment loss of H by diffusion through the host mineral can also contribute to

51   the pressure decrease (Bucholz et al., 2013). The decrease in pressure leads to formation of a

52   vapor bubble in the melt inclusion, and such bubbles are commonly referred to as shrinkage

53   bubbles because of the process that forms them (e.g., Roedder, 1984). Because the solubility of

54   CO_2 in silicate melt is much lower than that of H_2O, resulting in a relatively high vapor-melt

55   partition coefficient for CO_2, formation of a shrinkage bubble can strongly deplete the coexisting

56   melt of dissolved CO_2 that was present at the time of entrapment.

57   For olivine-hosted melt inclusions, a decrease in temperature of 100°C is estimated to

58   create a shrinkage bubble that is 0.9 to 1.6 vol% of the inclusion (Anderson and Brown 1993;

59   Riker 2005; Ruscitto et al., 2011). These estimates include both the effect of melt contraction

60   due to cooling and the volume loss resulting from post-entrapment crystallization of olivine on

61   inclusion walls. Further expansion of the shrinkage bubble occurs between eruption and

62   quenching as the melt continues to contract down to the glass transition temperature, but this

63   happens over such a short timescale that little to no additional volatiles are likely to diffuse from

64   the melt to the bubble (Anderson and Brown 1993).

65   Determining original CO_2 contents for melt inclusions with shrinkage bubbles requires

66   adding the mass of CO_2 in the bubble back into the inclusion. In addition to the experimental

67   method described here, this has been done by estimating the CO_2 contents of bubbles (Anderson

68   and Brown, 1993; Riker, 2005; Shaw et al., 2008; Steele-MacInnis et al., 2011) or by

69   measurement of the CO_2 density in the bubble using micro-Raman spectroscopy (Esposito et al.,

70   2011; Hartley et al., 2014; Moore et al., in review). In their study of Kilauea Iki melt inclusions,

71   Anderson and Brown (1993) estimated the amount of CO_2 that had been lost to shrinkage

72   bubbles. They estimated that most bubble-bearing melt inclusions at Kilauea Iki contained pre-

73   eruptive vapor bubbles that were ~0.5 vol% of the inclusion at their eruptive temperatures. The

74   uncertainty in this method is knowing the size of the vapor bubble at the time of eruption,

75   because cooling during eruption and quenching causes the vapor bubble to expand, but the

76   timescale is sufficiently rapid that little additional CO_2 is likely to transfer from melt to bubble.

77   To quantitatively investigate the loss of CO_2 into shrinkage bubbles, we experimentally

78   heated large melt inclusions in olivine from a Mauna Loa picrite in order to dissolve the vapor

79   back into the melt. Our results demonstrate that 40-90% of the initial CO_2 that was dissolved in

80   the melt inclusions was lost to the vapor bubble, with an average loss of 75%.

81

82   **Samples and Methods**

83   The olivine used in this study are from Puu Wahi, a 910 yr B.P. line of scoria cones

84   situated at ~3000 m elevation on the NE rift zone of Mauna Loa (Lockwood, 1995). The olivine

85   come from reticulite scoria and were naturally quenched to glass during eruption. Samples of

86   this material were collected in 1997 by Wallace and A.T. Anderson. Melt inclusions in the

87   olivine are commonly large (80-120 μm diameter), and all of the melt inclusions contain vapor

88   bubbles that are ≤3 vol% of the inclusion. We analyzed one set of naturally quenched inclusions

89   (n=8) and performed heating experiments on a different set of inclusions (n=12), all from the

90   same scoria clast. As will be shown below, the olivine and melt inclusions mostly have fairly

91   uniform compositions, making a comparison of heated vs. unheated inclusions useful for

92   assessing how much CO_2 is in the vapor bubbles. An alternative methodology would have been

4

Revision 1

93   to analyze individual melt inclusions by FTIR spectroscopy before and after heating, which can

94   be done if the inclusions are not intersected during initial sample preparation (e.g., Massare et al.,

95   2002). However, we chose not to use this approach because it does not allow the melt inclusion

96   major element composition to be measured before heating, and therefore it is not possible to

97   assess how post-entrapment crystallization has affected the volatile concentrations in the

98   unheated inclusions. Furthermore, when doing heating experiments on thick wafers that still

99   have MI fully enclosed, the chances of compromising inclusions by invisible cracks are very

100   high.

101   Melt inclusions from other Puu Wahi clasts have been used for experiments on H

102   diffusion through the olivine host (Gaetani et al., 2012) and for analysis of trace elements and Sr

103   isotopes, which are remarkably diverse (Sobolev et al., 2011). The latter study reports olivine

104   compositions of Fo_{82-89}. which is a much wider range than the olivine in the clast that we studied

105   ($Fo_{86.5-89.1}$).

106   Individual crystals were heated using a Vernadsky Institute heating stage with controlled

107   oxygen fugacity (Sobolev et al., 1980). All but one olivine were heated rapidly to 1420°C for

108   <10 minutes, which rehomogenized the vapor bubbles into the melt. Such a high temperature is

109   above the trapping temperatures (estimated below to be 1280°C) but was required to get the

110   vapor bubbles to rehomogenize quickly. After each inclusion was homogenized, power to the

111   furnace was turned off in order to quench the inclusion to glass. However, even with the very

112   rapid quenching that occurs in the Vernadsky stage, a vapor bubble formed in three of the melt

113   inclusions (h4, h5, h7; see Table 1) during quench. Both unheated and heated inclusions were

114   analyzed by FTIR spectroscopy and electron microprobe (Table 1).

5

Revision 1

115   To prepare the samples, the olivine host crystals were mounted on glass slides using

116   acetone-soluble, thermal-setting cement and ground into doubly polished wafers with two

117   parallel sides. The thickness of each melt inclusion was measured by mounting the edge of the

118   doubly polished olivine wafer to a needle using epoxy and immersing the wafer into a cylindrical

119   glass well filled with refractive index liquid (n = 1.657). This allows the crystal to be rotated and

120   viewed parallel to the flat dimension under a microscope with a calibrated eyepiece, thereby

121   allowing a direct measurement of the thickness. These measurements have an accuracy of ±1 to

122   ± 3 µm, depending on how close the inclusion is to the edge of the wafer.

123

124   *Infrared spectroscopy*

125   Transmission infrared spectra of the melt inclusion glasses were obtained using a Nicolet

126   Magna 560 Fourier Transform Infrared Spectrometer interfaced with a Spectra-Tech Nic-Plan

127   microscope at Texas A&M University. For each melt inclusion, three individual spectra were

128   taken using an adjustable rectangular aperture. All spectra were acquired using a KBr

129   beamsplitter and liquid-nitrogen-cooled $HgCdTe_2$ (MCT) detector.

130   The quantitative procedures and band assignments described in Dixon et al. (1995) were

131   followed for this work. Quantitative measurements of dissolved total H_2O and carbonate (CO_3^{2-})

132   were determined using Beer's law:

133
$$c = \frac{M\ A}{\rho\ d\ \varepsilon}$$

134   where c is the concentration (in weight fraction) of the absorbing species, M is the molecular

135   weight (18.02 for total H_2O; 44.00 for CO_2), A is the absorbance intensity of the band of interest,

6

Revision 1

136   ρ is the room temperature density of the glass, d is the thickness, and ε is the molar absorption

137   coefficient.

138   Total dissolved H_2O was measured using the intensity of the broad, asymmetric band

139   centered at 3530 cm^{-1}, which corresponds to the fundamental OH-stretching vibration. The

140   absorbance intensity (peak height) was measured graphically from printed spectra, and the total

141   H_2O concentration was calculated using an absorption coefficient of 63 ± 3 L/mol cm (Dixon et

142   al., 1995). Precision of the H_2O analyses is about $\pm 5\%$.

143   Dissolved carbonate was measured from the absorbances of the bands at 1515 and 1430

144   cm^{-1}, which correspond to antisymmetric stretching of distorted carbonate groups (Fine and

145   Stolper, 1986; Dixon et al., 1995). Because the shape of the background in the region of the

146   carbonate doublet is complex, absorbance intensities for the 1515 and 1430 cm^{-1} bands were

147   measured after subtraction of a reference spectrum for a decarbonated basaltic glass so as to

148   achieve a relatively flat background (Dixon et al., 1995). The molar absorptivity for carbon

149   dissolved as carbonate in basaltic glasses is compositionally dependent (Dixon and Pan, 1995).

150   Dissolved carbonate contents (reported in Table 1 and hereafter as the equivalent amount of CO_2,

151   in ppm) were determined using molar absorption coefficients of 353 ± 4 L/mol cm (for unheated

152   inclusions) and 360 ± 7 L/mol cm (for heated inclusions), calculated from the average

153   compositions of the glasses and the equation reported by Dixon and Pan (1995). Precision of the

154   carbonate analyses is about $\pm 20\%$.

155   One experimentally heated melt inclusion (PW_h1) had CO_2 below the detection limit

156   (~25 ppm) and was quite anomalous in this regard compared to the other heated inclusions. This

157   melt inclusion also had a very low S content. We do not consider this inclusion further in our

7

Revision 1

158   analysis because of the likelihood that it formed originally at anomalously low pressure

159   compared to the other inclusions.

160

161   *Electron Microprobe*

162   Major elements and S were analyzed in all glasses with a Cameca SX-50 electron

163   microprobe at Texas A&M University using mineral and glass standards. Analytical accuracy

164   was assessed by analysis of U.S. National Museum glass standard VG-2. Sulfur was analyzed

165   using an anhydrite standard, 60 s on-peak counting time, and a S K_α wavelength offset measured

166   on pyrite, which corresponds approximately to the $S^{6+}/\sum S$ ratio expected for a basaltic glass

167   equilibrated at the FMQ oxygen buffer (Wallace and Carmichael, 1994). Analyses of glass

168   standard VG-2 using this procedure yielded a S concentration of 0.137 ± 0.006 wt% (n=11),

169   similar to the value reported by Dixon et al. (1991) and Dixon and Clague (2001). The values

170   reported in Table 1 are the averages of analyses of 3 spots on each melt inclusion. One standard

171   deviation uncertainties based on replicate analyses are equal to the following amounts, in wt%:

172   SiO_2 (0.17), TiO_2 (0.08), Al_2O_3 (0.08), FeO (0.15), MnO (0.02), MgO (0.06), CaO (0.10), Na_2O

173   (0.06), K_2O (0.01), P_2O_5 (0.02), and S (0.008).

174

175   **Results**

176   Photomicrographs of unheated and heated melt inclusions are shown in Figure 1. As

177   described above, temperatures well above the original trapping temperature were required to get

178   the vapor bubbles to rehomogenize quickly. It is likely that using longer heating times would

179   have yielded lower homogenization temperatures because it would have allowed dissolved

180   volatile contents, particularly slowly diffusing CO_2, to reach equilibrium concentrations by

8

Revision 1

181 diffusion throughout the inclusion, but the short times were needed to minimize any loss of H by

182 diffusion through the olivine. In addition, the fact that the pre-experiment bubble vol% values

183 were small (≤3 vol%) and in a fairly narrow range and that the bubble in each inclusion

184 homogenized at a similar temperature suggest that none of the bubbles were primary bubbles that

185 had been heterogeneously trapped with melt (Roedder , 1984). The presence of primary bubbles

186 would likely have caused a larger range in bubble vol% values (e.g., Moore et al., 2014) and

187 consequently, much more variable homogenization temperatures and/or inclusions that could not

188 be rehomogenized.

189   The compositions of the unheated and heated melt inclusions are shown on a diagram of

190 FeO^T vs. MgO in Figure 2. The unheated melt inclusions are relatively uniform in composition.

191 The host olivine compositions are also relatively uniform, with average Fo contents of 88.1 ± 0.2

192 in the unheated inclusions and 88.1 ± 0.7 in the heated inclusions. Assuming an olivine-melt K_d

193 value of 0.3 (Roeder and Emslie, 1970) and FeO/FeO^T of 0.85 (approximately FMQ), the

194 analyzed compositions of the unheated inclusions are predicted to be in equilibrium with Fo 86.4

195 olivine.   This is an indication that the melt inclusions were affected by post-entrapment

196 crystallization (PEC). Addition of equilibrium olivine in 0.1 wt% increments requires ~4%

197 olivine added to restore the melt inclusion compositions to equilibrium with $Fo_{88.1}$ olivine. Also

198 shown in Figure 2 are the compositions of submarine glasses from the SW rift zone of Mauna

199 Loa (Garcia et al., 1995) and whole rock and matrix glass separates for the 1852 and 1868

200 subaerial picritic eruptions on Mauna Loa (Rhodes, 1995). The bulk rock picrite analyses show

201 the effects of variable olivine accumulation and thus plot along an olivine control line. The fact

202 that the PEC-corrected, unheated melt inclusion compositions fall below the trend shown for the

203 picrite data suggests that the inclusions were affected by Fe diffusive loss (Danyushevsky et al.,

9

Revision 1

204   2000), which also causes the true extent of PEC to be greater than calculated above for the case

205   of no Fe loss. Correction for the effects of both Fe loss and PEC for the unheated melt inclusions

206   yields an average initial melt inclusion composition with 11.7 wt% MgO and 10.8 wt% FeO^T and

207   an average PEC estimate of 9.6 wt% olivine.

208   The analyzed compositions of the heated melt inclusions show much higher MgO (16-

209   21.3 wt%) and slightly higher FeO^T (9.5-11.3 wt%) than the unheated inclusions. This makes

210   them in equilibrium with $Fo_{92.8}$ olivine, much higher than the actual host values. This is an

211   indication that the experimental temperatures were above the original trapping temperatures,

212   resulting in large amounts of olivine dissolution from the walls of the inclusions during the

213   heating experiment. To correct the H_2O and CO_2 contents of the heated inclusions to be

214   comparable to the corrected values for the unheated inclusions, we used elements that are

215   incompatible in olivine (Ti, Al, Ca, K, P). We used the concentrations of these elements in each

216   heated melt inclusion and the concentration in the average PEC and Fe-loss corrected

217   composition for the unheated inclusions to calculate the excess olivine dissolved from the

218   inclusion-host interface during the experimental heating according to the relationship:

219

220   wt% element in original trapped melt / wt% element, measured = 1 + wt. fraction excess olivine

221

222   The results indicate that 22-43 wt% excess olivine (relative to the initial mass of melt) was

223   dissolved during the experiments. This means that the concentrations of CO_2 and H_2O in the

224   heated melt inclusions were diluted by the large amount of dissolved olivine caused by the

225   overheating. We have corrected the concentrations using the equation above and the values for

226   excess olivine dissolved for each heated inclusion calculated from the Ti, Al, Ca, K, and P data.

10

Revision 1

227   It should be noted, however, that there can be significant heterogeneity in minor and trace

228   elements within Hawaiian melt inclusions from a given sample (e.g., Sides et al., 2014), and this

229   causes additional uncertainty in our calculation of excess olivine dissolved.

230   Even before accounting for the dilution effect caused by olivine dissolution, it is evident

231   that the CO_2 concentrations (as measured) in the heated inclusions are significantly greater than

232   those in the unheated inclusions (Table 1). After recalculation, as described above, to correct for

233   the dilution effect, the CO_2 contents of the heated inclusions are 224-505 ppm (n=11), much

234   higher than the CO_2 contents of the naturally quenched inclusions (38-158 ppm; n=8), all of

235   which contain shrinkage bubbles (Fig. 3). The three melt inclusions in which shrinkage bubbles

236   re-formed during quenching are at the lower end of the range of CO_2 values, but other bubble-

237   free inclusions have similar and even lower values. The fact that vapor bubbles sometimes

238   reformed is probably caused by the large difference between the peak heating temperature and

239   the glass transition temperature, which results in extensive melt contraction relative to the olivine

240   host during experimental quenching. This causes pressure to drop precipitously in a bubble-free

241   melt inclusion (e.g., Lowenstern, 1995). Therefore, even though the heated melt inclusions had

242   dissolved substantial excess olivine and were therefore not vapor saturated at the beginning of

243   quenching, the melt contraction and consequent large pressure drop would be sufficient to cause

244   a vapor bubble to form. However, the experimental quenching time is rapid enough that very

245   little CO_2 should diffuse into the bubble from the surrounding melt.

246   Dissolved H_2O contents of the melt inclusions, both heated and unheated, are very

247   uniform (0.32 ± 0.02 wt% for unheated, 0.29 wt% ± 0.02 for heated, after correction for dilution

248   effect). This indicates that minimal to no diffusive loss of H_2O occurred during the short heating

249   time (e.g., Gaetani et al., 2012), despite the very high experimental temperatures. The slight

11

250   difference between the two groups could be caused by uncertainties in the correction procedures.

251   Our results demonstrate that substantial CO_2 is lost to shrinkage bubbles that form post-

252   entrapment. A comparison of the average CO_2 content of heated inclusions (330 ppm ± 90) and

253   unheated inclusions (90 ppm ± 50) indicates that 40-90% of the initial CO_2 that was dissolved in

254   the melt inclusions was lost to shrinkage bubbles, with an average loss of 75%. These results are

255   comparable to values estimated using micro-Raman spectroscopy on Solchiaro (Italy), Kilauea,

256   and Laki (Iceland) melt inclusions (Esposito et al., 2011; Moore et al., in review; Hartley et al.,

257   2014).

258   Based on our results, it is clear that accurate pressures of trapping cannot be determined

259   unless the CO_2 in shrinkage bubbles has been quantified. Pressures of melt inclusion entrapment

260   calculated using the H_2O and CO_2 data for the corrected, heated inclusions range from 0.5 to 1.1

261   kbar (Fig. 4; pressures calculated using VolatileCalc; Newman and Lowenstern, 2002). For

262   comparison, pressures calculated for the unheated samples are 0.09 to 0.35 kbar. The H_2O and

263   CO_2 variations in the heated inclusions are consistent with a degassing path (either closed- or

264   open-system), which follows a vertical trajectory on a diagram of CO_2 vs. H_2O for melts with

265   low H_2O concentration. This conclusion holds true even if the three melt inclusions that had

266   bubbles re-form on quench are excluded. These results suggest that the olivine from a single

267   scoria clast crystallized over a range of depths (~1.8-3.9 km for a crustal density of 2800 kg/m^3),

268   trapping variably degassed melts. This does not require that the olivine crystallized during

269   closed-system ascent of a single batch of magma, as it is possible that they were pre-existing

270   crystals, originally formed at various depths, that were entrained by rising melts. However, the

271   narrow range of host olivine and melt inclusion compositions for the clast that we studied

272   implies a close relationship or similar origin for the olivine.

12

Revision 1

273

Computational methods for assessing CO$_2$ lost to shrinkage bubbles

In the absence of experimental heating studies or direct measurement of CO$_2$ density in shrinkage bubbles by micro-Raman spectroscopy (Esposito et al., 2011; Hartley et al., 2014; Moore et al., in review), it is possible to estimate the amount of CO$_2$ that is in the bubbles. In this section we evaluate the accuracy of such estimates based on a comparison with our experimental results. It is important to note, however, that carbonate mineral phases have been detected on the walls of bubbles in some melt inclusions (Kamenetsky et al., 2001, 2002, 2007; Moore et al., in review). Because the C in these carbonates is probably derived from CO$_2$ in the vapor bubble, the computational methods for estimating CO$_2$ lost to vapor bubbles may be accurate for melt inclusions that contain carbonates. In addition to carbonates in vapor bubbles, anomalously high C contents have been documented at the inclusion-host interface in some melt inclusions analyzed by SIMS using depth profiling (i.e., inclusions that were not exposed prior to analysis; Esposito et al., 2014). This could indicate that a thin film of CO$_2$-rich gas or carbonates is present in cracks along the inclusion-host interface as a result of differential shrinking of the melt and host crystal during quenching. Because experimental heating and homogenization are able to fully redissolve all of the CO$_2$ that was originally present in a melt inclusion at trapping (as long as the heating time is sufficient to redissolve any carbonate mineral phases), our results are valuable for testing the usefulness of computational methods used to infer original CO$_2$ contents.

As discussed previously, the major uncertainty in computational methods is knowing the size of the vapor bubble at the time of eruption, because cooling during eruption and quenching causes the vapor bubble to expand, but the timescale is sufficiently rapid that little additional

13

Revision 1

296 CO_2 is probably lost from melt to bubble. In their study of Kilauea Iki melt inclusions, Anderson

297 and Brown (1993) estimated that most bubble-bearing melt inclusions contained pre-eruptive gas

298 bubbles of 0.5 vol% of the inclusion at their eruptive temperatures. Riker (2005) used phase

299 equilibrium calculations together with volume and thermal expansion data for silicate melts and

300 olivine to estimate a relationship for Mauna Loa tholeiitic melts describing the vol% bubble

301 formed due to cooling and post-entrapment crystallization as a function of the difference

302 between the trapping and pre-eruption temperatures. The resulting equation was:

303 $$\text{Bubble vol\%} = 0.0162 \, \Delta T$$

304

305 where $\Delta T = T_{trapping} - T_{pre\text{-}eruption}$. For the Puu Wahi melt inclusions, we estimate trapping and

306 eruption temperatures using the experimentally calibrated thermometer of Montierth et al. (1995)

307 based on melt MgO content. For the unheated inclusions, the composition corrected for effects

308 of PEC and Fe loss has 11.7 wt% MgO, yielding a trapping temperature of 1280°C. The

309 temperature at the time of eruption can be estimated using the actual analyzed glass MgO values

310 of the unheated inclusions, yielding a temperature of 1203°C. For ΔT of 77°C, we calculate that

311 the pre-eruption bubble size for the Puu Wahi melt inclusions would have been 1.25 vol% using

312 the Riker (2005) relationship.

313   Using this value for the pre-eruption bubble volume, we estimate how much CO_2 the

314 vapor bubbles would have contained just prior to eruption. By adding this estimated mass of CO_2

315 back into each inclusion, we can estimate the concentration that the melt would have had at the

316 time of trapping. To do this for each inclusion, we used the VolatileCalc program (Newman and

317 Lowenstern, 2002) to estimate the pressure of the inclusion and the mol% CO_2 in the vapor

318 bubble at the pre-eruption temperature using the dissolved concentrations of H_2O and CO_2, and

14

Revision 1

319   we used the Redlich-Kwong equation of state to determine the molar volume of CO_2 in the vapor

320   bubble.   In the Redlich-Kwong calculations, we ignored the effect of H_2O on the P-V-T

321   properties of the mixed-volatile vapor phase because the vapor is nearly pure CO_2 (see Table 1).

322   The results are given in Table 1 and shown in Figure 3 for comparison with the heated

323   inclusions. The assumption of a 1.25 vol% pre-eruption bubble results in an estimated loss of

324   75% CO_2 to the shrinkage bubble, which agrees well with the % loss values that we estimate by

325   comparing the CO_2 in the heated inclusions with those of the unheated inclusions.

326   As a further test, we created a forward model of the relationship between bubble vol%

327   and the fraction of CO_2 lost to a bubble for a melt starting with 0.3 wt% H_2O and 340 ppm CO_2,

328   the average of the heated melt inclusions (Fig. 5). The model uses a closed-system degassing

329   calculation from VolatileCalc to simulate the effect of post-entrapment decompression in a melt

330   inclusion. The use of VolatileCalc in this regard is a simplification because in a melt inclusion,

331   the decompression occurs due to cooling-induced crystallization and melt contraction whereas in

332   VolatileCalc the decompression occurs isothermally. Furthermore, in the natural system that we

333   are simulating (Puu Wahi melt inclusions), post-entrapment crystallization of about 10 wt%

334   olivine causes a small increase in dissolved volatiles in the inclusion, and we have ignored this

335   effect as well. The calculations were done at 1200°C, and for simplicity we assumed a constant

336   melt density of 2800 kg/m^3 (i.e., the calculations do not include the change in density of silicate

337   melt, which is quite small over the pressure range considered) and we ignored the effect of the

338   compressibility of olivine, which is also quite small. For each step of decreasing pressure in the

339   closed-system degassing calculation, we calculated the mass and volume (using Redlich-Kwong,

340   again ignoring the effect of H_2O on the P-V-T properties of the mixed volatile phase) of CO_2 that

341   had exsolved from the melt and the mole fractions of CO_2 and H_2O in the vapor phase. For an

15

342   assumed initial mass of a single phase melt inclusion at time of trapping, these values at each

343   pressure step can be converted to vol% vapor bubble inside the inclusion. The results (Fig. 5)

344   show that when the vapor bubble reaches 1.25 vol% of the inclusion, ~77% of the initial

345   dissolved CO_2 has been lost to the bubble, and the internal pressure of the inclusion has dropped

346   from 740 bars to ~200 bars. This agrees very well with the pre-eruptive bubble volume for the

347   Puu Wahi melt inclusions calculated using Riker (2005) and the estimate of the fraction of initial

348   CO_2 lost to the vapor bubbles based on our heating experiments.

349   Given this agreement, we conclude that the Riker (2005) method for estimating the pre-

350   eruption bubble size for Hawaiian tholeiitic melts gives reliable results, in the absence of actual

351   heating experiments or measurement of CO_2 densities in the inclusions by Raman spectroscopy.

352   Based on the discussion above, we conclude that the fraction of the initial dissolved CO_2 in a

353   melt inclusion that is lost to a shrinkage bubble (and any subsequently formed carbonates) is

354   controlled by three factors: (1) the difference between the trapping and pre-eruption

355   temperatures, which controls both the extent of differential shrinkage between melt and bubble

356   and the extent of post-entrapment crystallization; (2) the trapping pressure; and (3) the initial

357   H_2O and CO_2 contents of the melt, which determine the mole fraction of CO_2 in the vapor phase

358   inside the bubble. In addition to these factors, Bucholz et al. (2013) have shown experimentally

359   that diffusive H loss can also contribute to vapor bubble formation because of the increase in

360   melt density caused by the loss of H_2O. Thus the extent of post-entrapment diffusive loss will

361   also affect how much dissolved CO_2 is lost to a shrinkage bubble. One consequence of the third

362   factor is that the effect of CO_2 loss to a shrinkage bubble is expected to be smaller for more H_2O-

363   rich melt inclusions than those studied here because the vapor bubble in such inclusions will

364   have lower mole fractions of CO_2 than the low-H_2O inclusions in our study. As a result, the

365   predicted relationship shown in Figure 5 will change for melts with different H_2O values (cf.

366   Steele-MacInnis et al., 2011).

367

368   **Crystallization depths for Hawaiian picrites**

369   Our results indicate that olivine crystallized at very shallow depths (~2 to 4 km) beneath

370   the surface of Mauna Loa. Large fluid inclusions ($\leq$100 μm in diameter) in some Puu Wahi

371   olivine appear to contain relatively low density CO_2 based on petrographic observations,

372   consistent with the interpretation based on melt inclusions that olivine crystallized at low

373   pressures. Such surprisingly low pressures of crystallization have also been inferred for olivine

374   erupted in the 1959 Kilauea Iki picrite (mostly less than 4 km; Anderson and Brown, 1993) and

375   for abundant Fo_{88-90} olivine in the Keanakakoi ash deposits at Kilauea (Hart and Wallace, 2000)

376   based on computational methods for restoring CO_2. Eruptions of olivine-rich lava are relatively

377   rare on the subaerial portions of both Kilauea and Mauna Loa but are more common on the

378   submarine parts of both volcanoes. As has been proposed for Kilauea Iki (Helz, 1987; Anderson

379   and Brown, 1993), the eruption of olivine-rich lava high on the NE rift zone of Mauna Loa

380   probably resulted from magma following an unusual pathway to the surface, thus bypassing

381   mixing and density filtering within the summit magma system.

382   Anderson (1995) demonstrated that exsolved CO_2 in picritic magmas plays an important

383   role in making them buoyant enough to be eruptible. For Hawaiian picritic magma, an initial

384   bulk CO_2 content of 0.3 wt% is sufficient to make the magma buoyant relative to degassed

385   tholeiitic basaltic magma at pressures of 2 kbar or less, but at higher pressures the picritic magma

386   is negatively buoyant because of the compressibility of the vapor phase. Thus Anderson (1995)

387   concluded that the rarity of erupted picrites at Hawaii is likely because primitive magma

17

Revision 1

388   typically enters the large summit reservoirs near their base, where the pressure is sufficiently

389   high to cause the bulk density of parental magma to be greater than that of stored magma.

390   Regardless of the mechanism, however, our new experimental results confirm that high-Mg

391   olivine phenocrysts can crystallize at shallow depths beneath Hawaiian volcanoes.

392

393   **Implications**

394   Our results for experimentally heated melt inclusions indicate that 40-90% of the initial

395   CO_2 that was dissolved in the melt inclusions at the time of trapping was lost to shrinkage

396   bubbles, with an average loss of 75%. Calculated trapping pressures for heated melt inclusions

397   (0.5-1.1 kbar) are significantly higher than the pressures calculated based only on the dissolved

398   CO_2 in the naturally quenched inclusions (0.09-0.35 kbar). To accurately infer original pressures

399   of crystallization and trapping for melt inclusions with shrinkage bubbles, the mass of CO_2 in the

400   bubbles must be either measured or calculated. This can be done by rehomogenization

401   experiments like those described here or through the application of micro-Raman spectroscopy.

402   In the absence of either of these approaches, we have shown that the method of Riker (2005) for

403   estimating pre-eruption bubble size is successful for estimating how much CO_2 is in shrinkage

404   bubbles in melt inclusions from Hawaiian tholeiitic magmas. For other melt compositions,

405   particularly those with higher H_2O contents, published olivine-melt thermometers could be used

406   to calibrate similar relationships between post-entrapment cooling, extent of crystallization, and

407   the volume % bubble that forms as a result. The effect of CO_2 loss to shrinkage bubbles is

408   expected to be smaller for more H_2O-rich melt inclusions than those studied here because the

409   vapor bubble in such inclusions will have lower mole fractions of CO_2 than the low-H_2O

410   inclusions in our study.

18

Revision 1

411

417

418   **References**

419   Anderson, A.T. (1974) Evidence for a picritic, volatile-rich magma beneath Mt. Shasta,

420   California. Journal of Petrology, 15, 243-267.

421   Anderson, A.T. (1995) CO_2 and the eruptibility of picrite and komatiite. Lithos. 34, 19-25.

422   Anderson, A.T., and Brown GG (1993) CO_2 contents and formation pressures of some Kilauean

423   melt inclusions. American Mineralogist, 78, 794-803

424   Bucholz, C. E., Gaetani, G. A., Behn, M. D., and Shimizu, N., (2013) Post-entrapment

425   modification of volatiles and oxygen fugacity in olivine-hosted melt inclusions. Earth and

426   Planetary Science Letters, 374, 145-155.

427   Danyushevsky, L.V., Della-Pasqua, F.N., and Sokolov, S. (2000) Re-equilibration of melt

428   inclusions trapped by magnesian olivine phenocrysts from subduction-related magmas:

429   petrological implications. Contributions to Mineralogy and Petrology, 138, 68-83.

430   Danyushevsky, L.V., McNeill, A.W., and Sobolev, A.V. (2002) Experimental and petrological

431   studies of melt inclusions in phenocrysts from mantle-derived magmas: an overview of

432   techniques, advantages, and complications. Chemical Geology, 183, 5-24.

19

Revision 1

433   Dixon, J.E., and Pan, V. (1995) Determination of the molar absortivity of dissolved carbonate in

434   basanitic glass. American Mineralogist, 80, 1339-1342.

435   Dixon, J.E., and Clague, D.A. (2001) Volatiles in Basaltic glasses from Loihi Seamount:

436   evidence for a relatively dry plume source. Journal of Petrology, 42, 627-654.

437   Dixon, J.E., Stolper, E.M., and Holloway, J.R. (1995) An experimental study of water and

438   carbon dioxode solubilities in Mid-Ocean Ridge basaltic liquids. Part I: calibration and

439   solubility models. Journal of Petrology, 36, 1607-1631.

440   Dixon, J.E., Clague, D.A., and Stolper, E.M. (1991) Degassing history of water, sulfur, and

441   carbon in submarine lavas from Kilauea Volcano, Hawaii. Journal of Geology, 99, 371-

442   394.

443   Esposito, R., Bodnar, R. J., Danyushevsky, L. V., de Vivo, B., Fedele, L., Hunter, J., Lima, A.,

444   and Shimizu, N. (2011) Volatile evolution of magma associated with the Solchiaro

445   eruption in the Phlegrean Volcanic District (Italy). Journal of Petrology, 52, 2431-2460.

446   Esposito, R., Hunter, J., Schiffbauer J.D., Shimizu N., and Bodnar, R. J. (2014) An assessment of

447   the reliability of melt inclusions as recorders of the pre-eruptive volatile content of

448   magmas. American Mineralogist, in press.

449   Fine, G., and Stolper, E. (1986) Carbon dioxide in basaltic glasses: concentrations and

450   speciation. Earth and Planetary Science Letters, 76, 263-278.

451   Gaetani, G.A., O'Leary, J.A., Shimizu, N., Bucholz, C.E., and Newville, M. (2012) Rapid

452   reequilibration of H_2O and oxygen fugacity in olivine-hosted melt inclusions. Geology,

453   40, 915-918.

454   Garcia, M.O., Hulsebosch, T.P., and Rhodes, J.M. (1995) Olivine-rich submarine basalts from

455   the southwest rift zone of Mauna Loa Volcano: Implications for magmatic processes and

20

456   geochemical evolution. In: Rhodes JM, Lockwood JP (eds) Mauna Loa Revealed:

457   Structure, Composition, History, and Hazards. American Geophysical Union,

458   Geophysical Monograph, 92, 219-239.

459   Hart, D., and Wallace, P.J. (2000) Volatiles in melt inclusions from the Keanakakoi Ash

460   Member, Kilauea Volcano: Implications for explosive Hawaiian eruptions. Eos,

461   Transactions American Geophysical Union, 81(46).

462   Hartley, M.E., Maclennan, J., Edmonds, M., and Thordarson, T. (2014) Reconstructing the deep

463   CO_2 degassing behaviour of large basaltic fissure eruptions. Earth and Planetary Science

464   Letters, 393, 120-131.

465   Helz, R. (1987) Diverse olivine types in lava of the 1959 eruption of Kīlauea volcano and their

466   eruption dynamics. USGS Professional Paper, 1350, 691-722.

467   Kamenetsky, V.S., Binns, R.A., Gemmell, J.B., Crawford, A.J., Mernagh, T.P., Maas, R., and

468   Steele, D. (2001) Parental basaltic melts and fluids in eastern Manus backarc basin:

469   Implications for hydrothermal mineralisation. Earth and Planetary Science Letters 184,

470   685-702.

471   Kamenetsky, V.S., Davidson P, Mernagh, T.P., Crawford, A.J., Gemmell, J.B., Portnyagin,

472   M.V., and Shinjo, R. (2002) Fluid bubbles in melt inclusions and pillow-rim glasses:

473   high-temperature precursors to hydrothermal fluids? Chemical Geology, 183, 349-364.

474   Kamenetsky, V.S., Pompilio, M., Metrich, N., Sobolev, A.V., Kuzmin, D.V., and Thomas, R.

475   (2007) Arrival of extremely volatile-rich high-Mg magmas changes explosivity of Mount

476   Etna. Geology, 35, 255-258.

21

477   Lockwood, J.P. (1995) Mauna Loa eruptive history – The preliminary radiocarbon record. In:

478   Rhodes JM, Lockwood JP (eds) Mauna Loa Revealed: Structure, Composition, History,

479   and Hazards. American Geophysical Union, Geophysical Monograph, 92, 81-94.

480   Lowenstern, J.B. (1995) Application of silicate-melt inclusions to the study of magmatic

481   volatiles. *In* Magmas, fluids and ore deposits. Thompson, J.F.H. (ed), pp. 71-100.

482   Massare, D., Metrich, N., and Clocchiatti, R. (2002) High-temperature experiments on silicate

483   melt inclusions in olivine at 1 atm: inference on temperatures of homogenization and

484   H_2O concentrations. Chemical Geology, 183, 87-98.

485   Metrich, N., and Wallace, P.J. (2008) Volatile abundances in basaltic magmas and their

486   degassing paths tracked by melt inclusions. *Minerals, Inclusions, and Volcanic*

487   *Processes*, Reviews in Mineralogy and Geochemistry, Mineralogical Society of America,

488   69, 363-402.

489   Montierth, C., Johnston, A.D., and Cashman, K.V. (1995) An empirical glass-composition-based

490   geothermometer for Mauna Loa lavas. In: Rhodes JM, Lockwood JP (eds) Mauna Loa

491   Revealed: Structure, Composition, History, and Hazards. American Geophysical Union,

492   Geophysical Monograph, 92, 207–217.

493   Moore, L., Gazel, E., Tuohy, R., Lloyd, A., Esposito, R., Hauri, E., Wallace, P. J., Plank, T., and

494   Bodnar, R. J. (2014) Bubbles matter: An assessment of the contribution of vapor bubbles

495   to melt inclusion volatile budgets. American Mineralogist, in review.

496   Newman, S., and Lowenstern, J.B. (2002) VolatileCalc: a silicate melt-H_2O-CO_2 solution model

497   written in Visual Basic Excel. Computers in Geosciences, 2, 597-604.

498   Rhodes, J.M. (1995) The 1852 and 1868 Mauna Loa picrite eruptions: Clues to parental magma

499   compositions and the magmatic plumbing system. In: Rhodes JM, Lockwood JP (eds)

Revision 1

500   Mauna Loa Revealed: Structure, Composition, History, and Hazards. American

501   Geophysical Union, Geophysical Monograph, 92, 241-262.

502   Riker, J. (2005) The 1859 eruption of Mauna Loa Volcano, Hawaii: Controls on the development

503   of long lava channels. Unpublished M.S. Thesis, University of Oregon.

504   Roedder, E. (1979) Origin and significance of magmatic inclusions. Bulletin de Mineralogie,

505   102, 467-510.

506   Roedder, E. (1984) Fluid Inclusions. Mineralogical Society of American, Reviews in

507   Mineralogy, 12, 646 p.

508   Roeder, P.L., and Emslie, R.F. (1970) Olivine-liquid equilibrium. Contributions to Mineralogy

509   and Petrology, 29, 275-289.

510   Ruscitto, D.M., Wallace, P.J., and Kent, A.J.R. (2011) Revisiting the compositions and volatile

511   contents of olivine-hosted melt inclusions from the Mount Shasta region: Implications for the

512   formation of high-Mg andesites. Contributions to Mineralogy and Petrology, 162, 109-132.

513   Shaw, A. M., Hauri, E. H., Fischer, T. P., Hilton, D. R., and Kelly, K. A. (2008) Hydrogen

514   isotopes in Mariana arc melt inclusions: Implications for subduction dehydration and the

515   deep-Earth water cycle. Earth and Planetary Science Letters, 275, 138–145.

516   Sides, I., Edmonds, M., Maclennan, J., Houghton, B.F., Swanson, D.A., and Steele-MacInnis,

517   M.J. (2014) Magma mixing and high fountaining during the 1959 Kilauea Iki eruption,

518   Hawaii. Earth and Planetary Science Letters, 400, 102-112.

519   Sobolev, A.V., Dmitriev, L.V., Barsukov, L.V., Nevsorov, V.L., and Slutskii, A.V. (1980) The

520   formation conditions of the high-magnesium olivines from the monomineralic fraction of

521   Luna 24 regolith. In: Lunar and Planetary Science Conference, 11th, Houston, TX,

522   Proceedings. Volume 1. Pergamon Press, 1980, p. 105-116.

523   Sobolev, A.V., Hofmann, A.W., Jochum, K.P., Kuzmin, D.V., and Stoll, B. (2011) A young

524   source for the Hawaiian plume. Nature, 476, 434-437.

525   Steele-MacInnis, M., Esposito, R., and Bodnar, R. J., (2011) Thermodynamic model for the

526   effect of post-entrapment crystallization on the H_2O-CO_2 systematics of vapor-saturated,

527   silicate melt inclusions. Journal of Petrology, 52, 2461-2482.

528   Wallace, P.J., and Carmichael, I.S.E. (1994) Sulfur speciation in submarine basaltic glasses as

529   determined by measurements of S$K\alpha$ X-ray wavelength shifts. American Mineralogist,

530   79, 161-167.

531

532   **Figure Captions**

533   **Fig. 1.** Photomicrographs of unheated and heated melt inclusions analyzed in this study. A 100

534   μm scale bar is shown at upper left. Note that some heated melt inclusions have a vapor bubble

535   that appeared during quenching. All vapor bubbles rehomogenized during the high temperature

536   heating experiment.

537

538   **Fig. 2.** FeO^T vs. MgO for unheated and heated melt inclusions. The average composition of the

539   unheated melt inclusions after correction for post-entrapment crystallization, with and without

540   the effects of Fe diffusive loss, are shown as open squares. Diagonal lines show equilibrium

541   values with various olivine compositions, as labelled. Shown for comparison are the

542   compositions of submarine glasses from the SW rift zone of Mauna Loa (Garcia et al., 1995) and

543   whole rock and matrix glass separates for the 1852 and 1868 subaerial picritic eruptions on

544   Mauna Loa (Rhodes, 1995).

545

24

Revision 1

546   **Fig. 3.** Histograms comparing CO_2 contents of **(A)** unheated and **(B)** heated melt inclusions,

547   after correction to compositions in equilibrium with $Fo_{88.1}$ olivine, as described in the text. Also

548   shown in **(A)** are estimated CO_2 contents of the unheated inclusions calculated by assuming a

549   1.25 vol% pre-eruptive bubble in each inclusion. The three inclusions in **(B)** in which bubbles re-

550   formed during quenching are marked with an X.

551

552   **Fig. 4.** H_2O and CO_2 concentrations of unheated and heated melt inclusions after correction to

553   compositions in equilibrium with $Fo_{88.1}$ olivine, as described in the text. Vapor saturation isobars

554   are calculated using VolatileCalc for a basaltic melt at 1280°C.

555

556   **Fig. 5.** Relationship between vapor bubble volume% and the fraction of initial dissolved CO_2

557   lost to the bubble, calculated as described in the text. Tick marks along the curve show the

558   internal pressure of the melt inclusion, in bars. The initial pressure at time of trapping (0.3 wt%

559   H_2O, 340 ppm CO_2) is 740 bars. The data point shows the average estimated pre-eruptive bubble

560   size for the Puu Wahi melt inclusions based on MgO content and calculated temperature (using

561   Riker, 2005) and the range in %CO_2 lost based on a comparison of heated and unheated

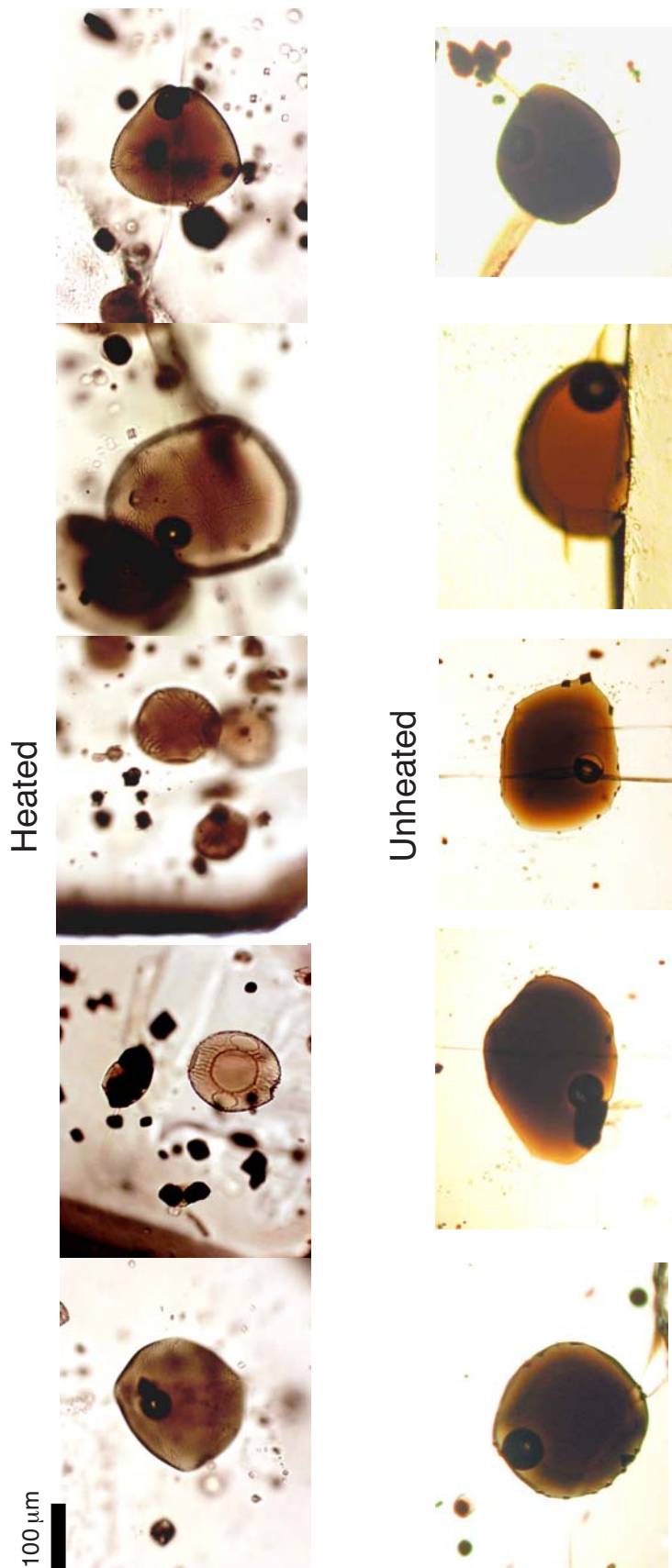562   inclusions. Vertical bar shows the range in % lost (40-90%) values.

563

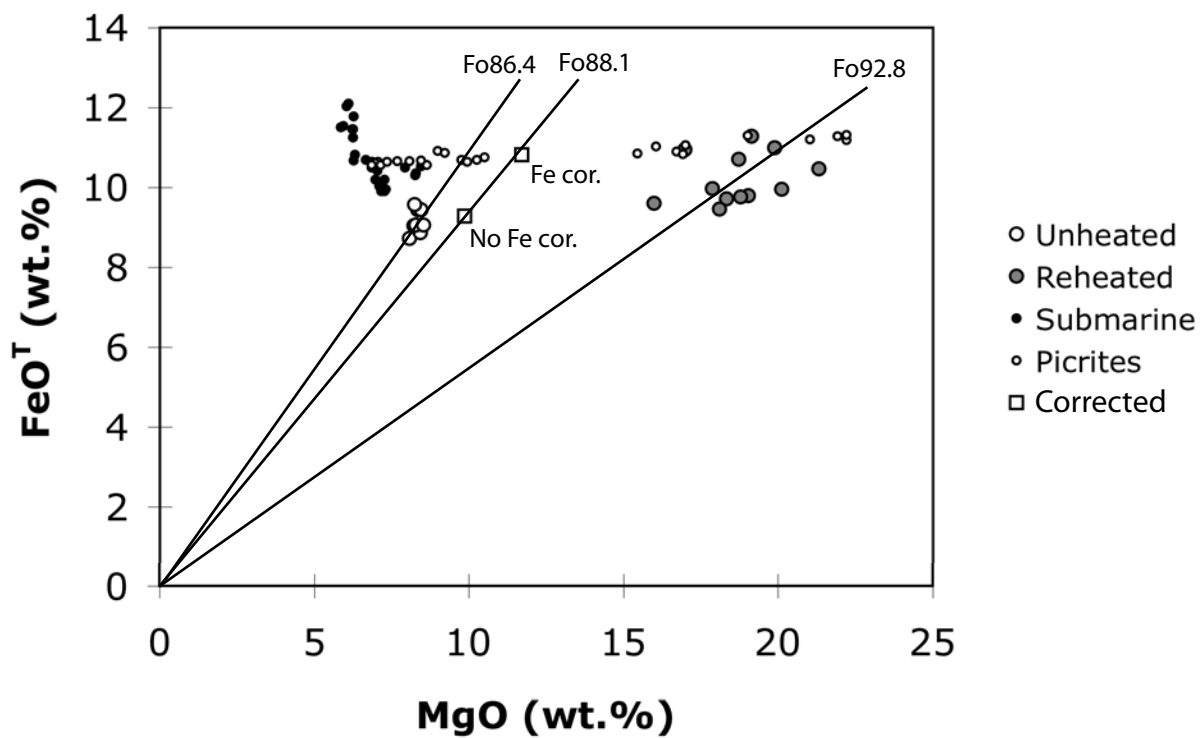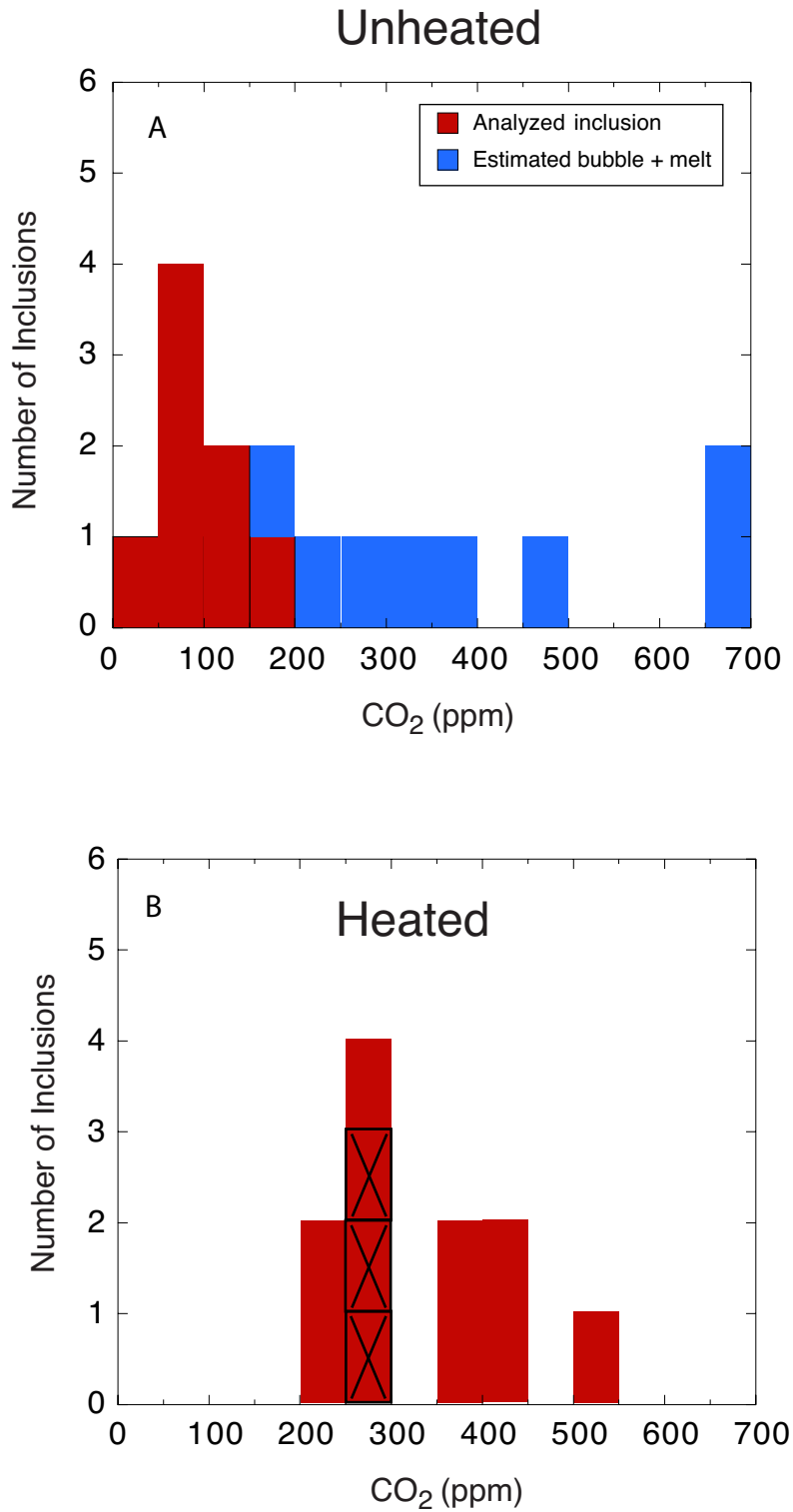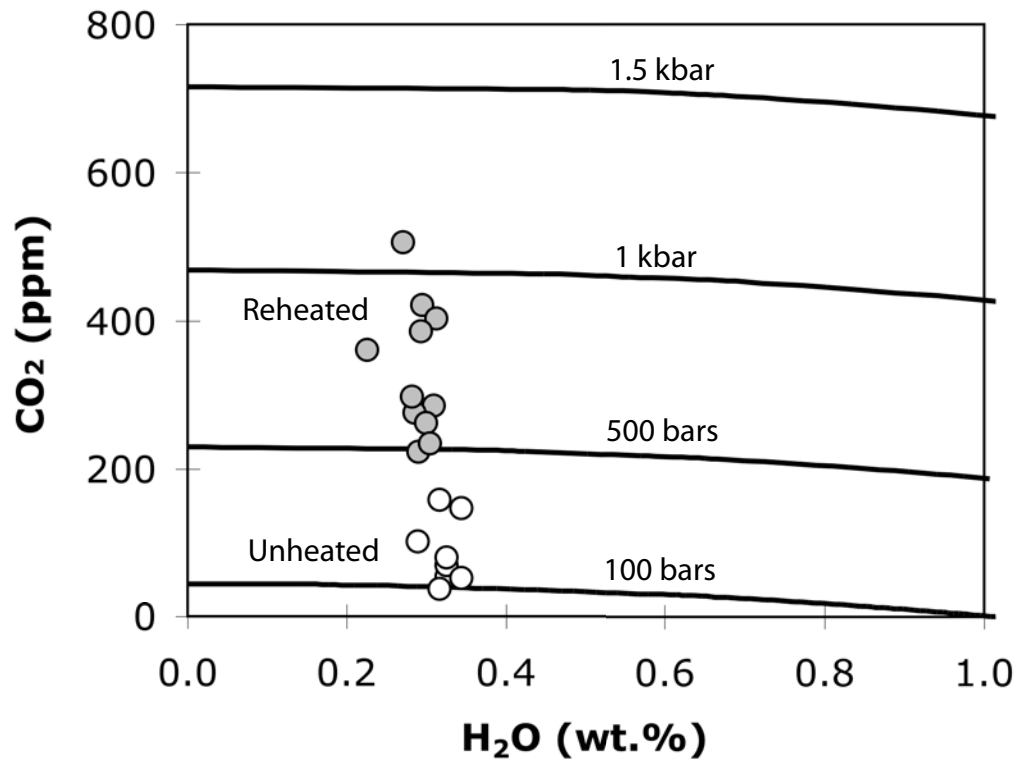564

25

Fig. 1

Fig. 2

Fig. 3

Fig. 4
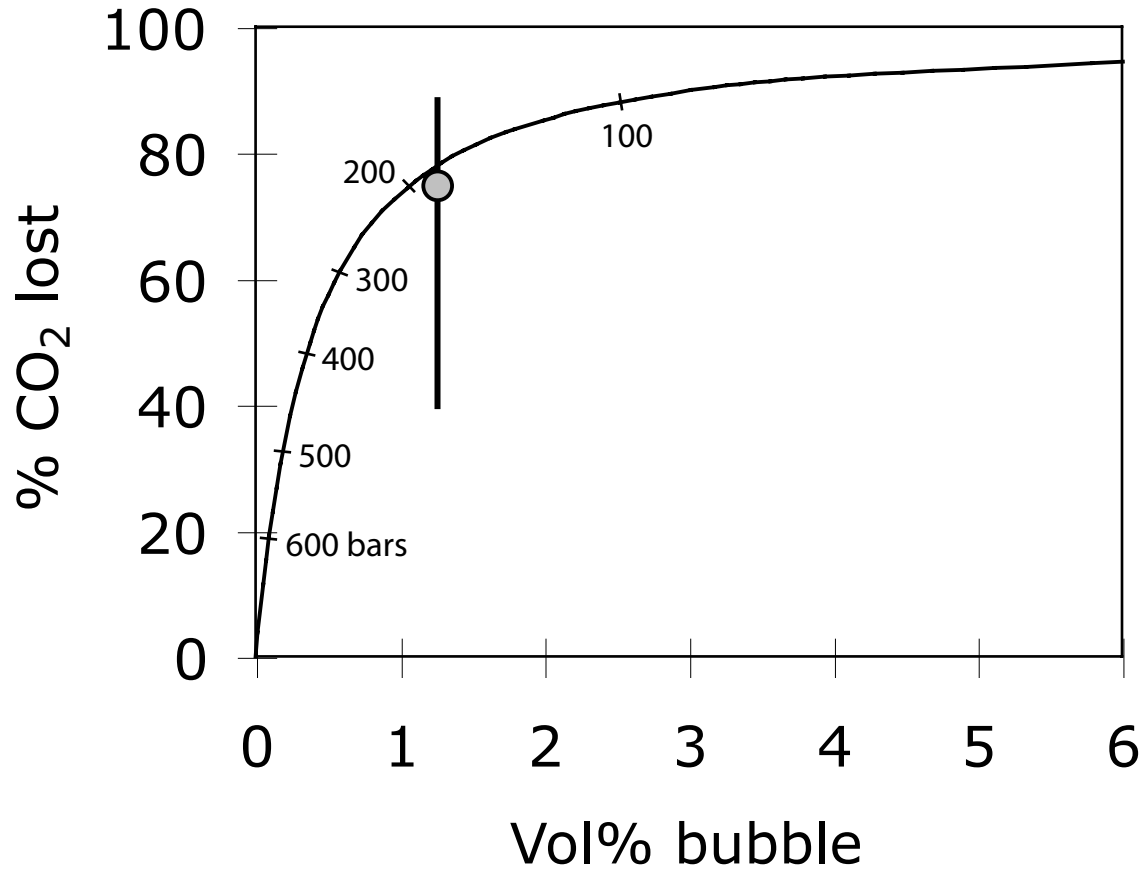
Fig. 5

Inclusion	Unheated k97_17_11	k97_17_21	k97_17_31	k97_17_41	k97_17_51	PC_11	PC_21	PC_31	Avg. Corr.
SiO2	52.81	52.40	52.59	53.08	52.39	52.35	51.71	52.48	50.71
TiO2	2.12	2.23	2.51	2.07	2.63	2.04	2.20	2.18	2.02
Al2O3	13.81	13.98	13.77	14.01	14.02	13.79	13.44	13.73	12.44
FeO	8.72	8.87	9.44	9.05	9.06	9.44	9.56	9.06	10.66
MnO	0.14	0.13	0.13	0.13	0.14	0.15	0.14	0.14	0.13
MgO	8.06	8.39	8.33	8.19	8.25	8.42	8.22	8.50	11.51
CaO	10.56	10.69	10.19	10.65	10.04	10.23	10.49	10.60	9.39
Na2O	2.29	2.29	2.45	2.33	2.49	2.35	2.18	2.28	2.10
K2O	0.46	0.44	0.46	0.29	0.68	0.42	0.49	0.39	0.41
P2O5	0.29	0.26	0.28	0.19	0.29	0.27	0.30	0.29	0.24
S	0.125	0.137	0.064	0.096	0.131	0.140	0.124	0.107	0.10
H2O	0.36	0.35	0.36	0.36	0.38	0.32	0.38	0.35	0.32
CO2	60	175	78	89	58	113	163	42	88
Total	99.74	100.17	100.57	100.45	100.49	99.92	99.22	100.12	100.00
Host Fo	88.0	88.2	88.1	88.2	88.5	88.0	87.7	88.2	88.1
H2O corr.	0.33	0.32	0.33	0.33	0.34	0.29	0.34	0.32	
CO2 corr.	54	158	71	80	52	102	147	38	
P sat (bars)	129	353	166	185	125	230	330	94	
Xv CO2	0.91	0.97	0.93	0.94	0.90	0.96	0.96	0.88	
CO2 restored	251	705	330	366	243	465	657	178	

Notes: All concentrations are in wt%, except for CO2 and CO2 restored, which are in ppm. Olivine host composition is given in mol% forsterite.
Column labelled Avg. Corr. is the average of unheated melt inclusions after correction for PEC and Fe loss.
H2O corr. and CO2 corr. are values for each inclusion corrected for PEC and Fe loss.
P sat is vapor saturation pressure calculated using VolatileCalc. Xv CO2 is mole fraction CO2 in the vapor phase.
CO2 restored is based on estimated pre-eruption bubble volume of 1.25 vol.% for each inclusion. See text for details.

Inclusion	Heated PW_h1	PW-h3A	PW_h3B	PW_h4	PW_h5	PW_h6	PW_h7	PW_h8	PW_h9	PW_h10	PW_h11	PW-h12
SiO2	49.95	49.61	49.13	51.01	50.04	51.16	50.08	49.01	49.55	49.74	48.29	49.12
TiO2	1.96	1.45	1.40	1.35	1.59	1.63	1.56	1.23	1.51	1.43	1.50	1.62
Al2O3	10.90	9.52	9.49	10.40	10.14	10.61	10.46	9.14	10.34	9.98	10.22	10.22
FeO	9.60	11.27	11.00	10.95	9.71	9.97	9.46	10.47	9.96	9.80	10.71	9.77
MnO	0.13	0.16	0.15	0.17	0.14	0.16	0.17	0.16	0.13	0.16	0.14	0.15
MgO	16.00	19.14	19.89	17.00	18.34	17.87	18.11	21.33	20.12	19.04	18.73	18.78
CaO	8.06	7.62	7.53	8.14	7.80	8.24	7.99	7.10	7.60	7.73	8.64	7.86
Na2O	1.82	1.42	1.55	1.36	1.71	1.60	1.71	1.47	1.67	1.60	1.39	1.62
K2O	0.34	0.27	0.28	0.24	0.25	0.25	0.26	0.29	0.30	0.24	0.20	0.25
P2O5	0.23	0.25	0.19	0.20	0.21	0.20	0.20	0.20	0.25	0.16	0.17	0.20
S	0.009	0.099	0.094	0.070	0.045	0.079	0.049	0.075	0.132	0.024	0.113	0.086
H2O	0.23	0.17	0.20	0.22	0.22	0.22	0.23	0.21	0.24	0.21	0.22	0.22
CO2	n.d.	278	370	207	210	230	201	159	340	162	282	294
Total	99.22	100.99	100.88	101.08	100.19	101.99	100.26	100.66	101.80	100.10	100.32	99.89
Host Fo	87.9	87.9	87.7	86.5	88.5	88.4	88.4	88.0	89.1	88.5	87.6	88.7
T heat	1390	1420	1420	1420	1420	1420	1420	1420	1420	1420	1420	1400
Bubble				yes	yes		yes					
H2O corr.	0.26	0.23	0.27	0.31	0.28	0.28	0.30	0.29	0.29	0.30	0.31	0.29
CO2 corr.	n.d.	361	505	286	276	298	263	224	422	234	403	386
P sat (bars)		776	1073	623	601	647	574	491	905	513	867	830
Xv CO2		0.99	0.99	0.98	0.99	0.99	0.98	0.98	0.99	0.98	0.99	0.99

Notes: T heat is the temperature of experimental heating. Bubble indicates the inclusions in which a bubble re-formed on quenching.